Nano Research 2017, 10(9): 3238–3247
DOI 10.1007/s12274-017-1643-y
Research Article
ISSN 1998-0124
CN 11-5974/O4

Giant enhancement and anomalous temperature dependence of magnetism in monodispersed $NiPt_2$ nanoparticles

Aixian Shan[1,4], Chinping Chen[1] (✉), Wei Zhang[2], Daojian Cheng[2] (✉), Xi Shen[3], Richeng Yu[3] (✉), and Rongming Wang[4] (✉)

[1] *Department of Physics, Peking University, Beijing 100871, China*
[2] *State Key Laboratory of Organic-Inorganic Composites, Beijing University of Chemical Technology, Beijing 100029, China*
[3] *Beijing National Laboratory for Condensed Matter Physics, Institute of Physics, Chinese Academy of Sciences, Beijing 100190, China*
[4] *School of Mathematics and Physics, University of Science and Technology Beijing, Beijing 100083, China*

Received: 23 February 2017
Revised: 20 April 2017
Accepted: 23 April 2017

© Tsinghua University Press and Springer-Verlag Berlin Heidelberg 2017

KEYWORDS
$NiPt_2$ nanoparticles,
magnetism,
X-ray absorption near-edge spectroscopy,
density functional theory calculations

ABSTRACT

A simple yet general one-step solvothermal method is applied to synthesize sub-7 nm monodispersed single-crystal $NiPt_2$ nanoparticles (NPs) with the morphology of truncated octahedrons in the alloying state of disordered atomic arrangements. The effective magnetic moments of these NPs exhibit an anomalous temperature dependency, increasing from approximately 0.9 μ_B/atom at 15 K to 1.9 μ_B/atom at 300 K. This is an increase by a factor of more than three compared with bulk Ni. On the basis of experiments involving X-ray absorption near-edge spectroscopy of the L3 edge for Pt and density functional theory calculations, the observed novel magnetism enhancement and its anomalous temperature dependence are attributed to the electron transfer arising from the thermal-activation effects.

1 Introduction

Bimetallic magnetic nanomaterials are important functional materials, as they are promising candidates for magnetic storage and biomedical and catalytic applications [1–5]. The magnetic properties of bimetallic nanoparticles (NPs) have been investigated experimentally and differ from those of the corresponding bulk materials, owing to the size, shape, and composition effects [6, 7]. For example, the magnetic-moment distributions of bulk NiPt alloys have been studied via high-field susceptibility, magnetization,

Address correspondence to Chinping Chen, cpchen@pku.edu.cn; Daojian Cheng, chengdj@mail.buct.edu.cn; Richeng Yu, rcyu@aphy.iphy.ac.cn; Rongming Wang, rmwang@ustb.edu.cn

and neutron-scattering experiments [8–10]. The magnetic moments and the Curie temperature depend on the concentration of Ni, especially at a low Ni content. In addition, these values differ for ordered and disordered alloys [10–12]. The magnetic properties of NiPt NPs, on the other hand, need further investigation and are expected to differ from those of the bulk material. There are few reports of regular magnetization measurements for NiPt NPs. For example, magnetizations were measured for $Ni_{31}Pt_{69}$ and $Ni_{50}Pt_{50}$ NPs approximately 3–4 nm in size [13]. It would be interesting and challenging to reveal the mechanism responsible for the magnetic behaviors by engineering the structures, compositions, or even morphologies of NiPt NPs. In particular, the electron-transfer effect is perhaps one of the greatest advantages of bimetallic structures, as it allows the tuning of the magnetic properties. However, more rigorous and direct investigations of this effect, especially with high-quality single-crystalline NPs, are required.

Temperature-dependent magnetic moments have been of considerable interest in the investigation of magnetic materials. In general, for paramagnetic (PM) or ferromagnetic (FM) materials, the magnetic moment of an atom is intrinsic and does not change with the temperature. However, there are very few observations in recent years revealing that the average magnetic moments are enhanced for bimetallic nanomaterials, such as CoRh [14], CoAu [15], CoPt, and FePt nanoalloys [16]. The magnitude of these reported enhancements is a few tens of percent. Charge-transfer effects are suggested as the mechanism. In addition, the effective magnetic moment determined for FM materials, such as Ni bulk and nanomaterials [17–19], and bimetallic AuNi core–shell NPs [20], from the saturation magnetization would decrease with the rising temperature below the Curie point, T_c. According to the Heisenberg model, this is caused by thermal disorder induced in the mutual alignment of the local magnetic moment [21]. This is a well-known classical property. Interestingly, the average magnetic moment of a PM or FM material increases with the rising temperature. This has never been observed or reported in the literature.

Herein, we report a facile yet general solvothermal method for synthesizing monodispersed single-crystal $NiPt_2$ NPs with truncated octahedrons less than 7 nm in diameter. Magnetization measurements, including $M(T)$ and $M(H)$, are performed. A giant enhancement in the average magnetic moments is observed for these $NiPt_2$ NPs. The anomalous temperature dependence of the magnetism, which increases with the temperature, is observed from 15 to 300 K. Direct evidence of electron transfer from Ni to Pt due to the thermal-activation effects is provided by an X-ray absorption near-edge spectroscopy (XANES) experiment of the L3 edge for Pt. The charge-transfer effect for the enhancement of the magnetism is revealed by density functional theory (DFT) calculations. We consider that the observed novel magnetism enhancement and its anomalous temperature dependence for these $NiPt_2$ NPs are caused by the electron transfer with the assistance of thermal activation effects.

2 Results and discussion

$NiPt_2$ NPs are synthesized using a facile solvothermal method by the reduction of nickel(II) acetylacetonate ($Ni(acac)_2$, 97.0%) and platinum(II) acetylacetonate ($Pt(acac)_2$, 49.3%–49.8% Pt) in an oleylamine (OAm) solution. Figure 1(a) shows the X-ray diffraction (XRD) pattern of the $NiPt_2$ NPs in the 2θ region between 20° and 80°. Reflection peaks are observed at 41.3° and 47.6°, corresponding to the (111) and (200) fundamental peaks of face-centered cubic (fcc) Pt (JCPDS no. 870647), respectively. The peaks are shifted to higher angles relative to Pt, indicating that Ni is incorporated into the Pt fcc structure, forming an alloy phase with a concomitant lattice contraction. The broad bump around 63° is attributed to the background described by the blue line. The scanning electron microscopy (SEM) image on the left side of Fig. 1(b) shows that the monodispersed $NiPt_2$ NPs are dispersed layer-wise on the flattened substrate. This implies the merit of self-assembly. The ones with a lighter shade are in a double layer. The high-resolution transmission electron microscope (HRTEM) images in the top right show the continuous lattice fringes throughout one $NiPt_2$ NP. This reveals a single-crystal structure for the $NiPt_2$ samples. The histogram in the bottom right indicates that the as-prepared $NiPt_2$ NPs had a narrow size distribution, with an average size of approximately

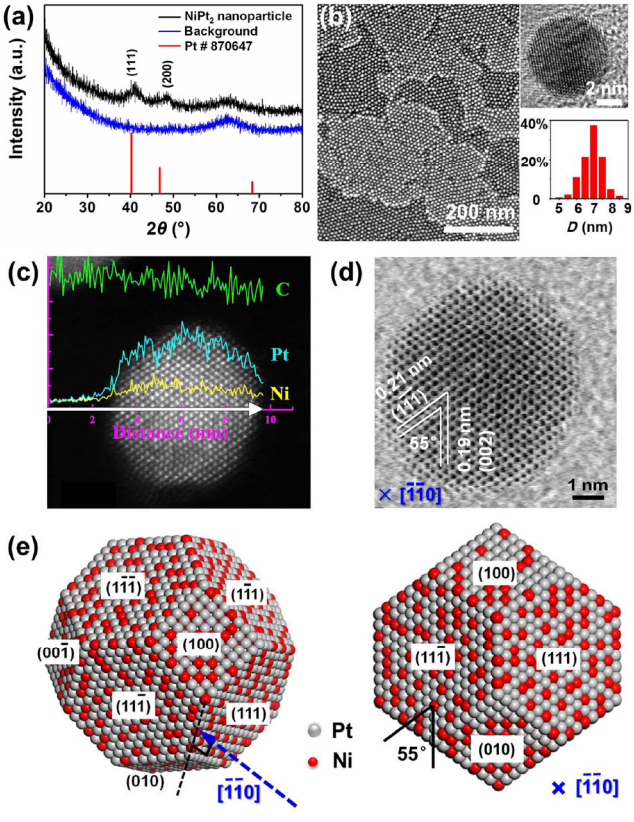

Figure 1 Characterizations of the structures of the $NiPt_2$ NPs. (a) XRD patterns for the as-prepared $NiPt_2$ NPs, background data curve, and the standard data of Pt (JCPDS no. 870647); (b) SEM image (left) showing the monodispersed $NiPt_2$ NPs in a self-organized order-array. The HRTEM image (top right) shows a single-crystal structure for the $NiPt_2$ NP. The size distribution is from 6 to 8 nm, as shown in the bottom right inset. (c) HAADF image and corresponding EDX line-scan profiles recorded for a single $NiPt_2$ NP, which reveal the distribution of the elements Ni, Pt, and C. The background signal indicating the element C is from the C film. (d) Corresponding BF image, along the [$\bar{1}\bar{1}$0] axis. (e) Equilibrium atomic structures of the $NiPt_2$ NP with a truncated-octahedral morphology, determined by SEMI-GCMC simulations using 8,000 atoms. The white and red spheres represent Pt and Ni atoms, respectively. The model illustration on the left shows the morphology of the truncated octahedron with a random arrangement of Ni and Pt atoms. The [$\bar{1}\bar{1}$0] axis is marked. An atomic model projected along the [$\bar{1}\bar{1}$0] view zone axis is shown on the right. It reconstructs the morphology and lattice structures of the corresponding HRTEM image shown in (d). The included angle for the two lattice planes—(002) and (1$\bar{1}\bar{1}$)—is 55°, well matching the corresponding one observed in (d).

7 nm. These results are obtained by statistically analyzing 324 NPs in the TEM images (shown in Fig. S1 in the Electronic Supplementary Material (ESM)). The energy dispersive X-ray spectroscopy (EDX) results shown in Fig. S2 (in the ESM) reveal that the NPs are composed of Ni and Pt. The atomic ratio of Ni:Pt is approximately 1:2, which is confirmed by inductively coupled plasma atomic emission spectrometry (yielded a ratio of 32:68).

Figure 1(c) shows the aberration-corrected high-angle annular dark-field (HAADF)-scanning transmission electron microscopy (STEM) image, with EDX line scan profiles of Ni, Pt and C for an individual $NiPt_2$ NP. The C signal appearing as a background is from the C film. The following two features are noted. First, the line-scan patterns are smoothed out, without a strong indication of spatially periodic structures. Second, regarding the HAADF-STEM image, the contrast usually depends on both the thickness and the atomic number; that is, a larger thickness and atomic number yield a brighter contrast. The HAADF-STEM contrast is linearly dependent on the thickness. In Fig. 1(c), there is a gradual isotropic change in the contrast from the center to the edge region. Obviously, this is due to the variations in the thickness. No appreciable alternating bright or dark spots appear. This indicates that the Ni and Pt atoms are homogeneously distributed, i.e., in a disordered arrangement. For an orderly arrangement of the alloy, one would expect far sharper and more periodic contrast between the Ni-rich and Pt-rich locations, as was reported for CoPt alloy crystals [22]. Figure 1(d) shows the bright field (BF) image, viewed along the [$\bar{1}\bar{1}$0] axis. The $NiPt_2$ NP has a truncated-octahedral shape and is approximately 7 nm in size. The lattice spacings correspond to the (1$\bar{1}\bar{1}$) and (002) planar distances of fcc crystalline Pt. The included angle for these two lattice planes is measured as approximately 55°. Figure 1(e) shows two images of the simulation isometric model with the truncated-octahedral structure. They are for the same truncated-octahedral NP viewed from different directions. The [$\bar{1}\bar{1}$0] view zone axis is marked specifically for the two images. The equilibrium structures of an $NiPt_2$ NP with 8,000 atoms are investigated via semi-grand-canonical ensemble Monte Carlo (SEMI-GCMC) simulations at 0 K. The white and red spheres represent Pt and Ni atoms, respectively. Regardless of whether the initial state had an ordered or disordered configuration, the final stable configurations for the structures of the $NiPt_2$ NPs are

in spatially disordered arrangements of Ni and Pt atoms (see Fig. 1(e)). The image on the right is obtained via projection along the [$\bar{1}\bar{1}$0] view zone axis. It corresponds to the same particle orientation in the STEM image of Fig. 1(d). The lattice arrangement and the included angle for the corresponding lattice planes are the same as those in Fig. 1(d). For instance, the included angle for the (002) and (1$\bar{1}\bar{1}$) lattice planes in the model image is 55°, which is equal to that shown in Fig. 1(d). Thus, the truncated-octahedral morphology of the $NiPt_2$ NP is confirmed.

The zero field-cooling (ZFC) and field-cooling (FC) $M(T)$ curves in Fig. 2(a) and the $M(H)$ curves in Fig. 2(b) indicate PM behavior at T > 12.5 K, instead of superparamagnetic (SPM) properties. The curve of $1/M$ vs. T in the left inset of Fig. 2(a) shows a straight line at approximately T > 100 K, which is a signature of perfect PM behavior. The deviation sets in gradually at a lower temperature, indicating that some of the magnetic moments behave differently from those of the perfect PM at a low temperature with the presence of, e.g., the ferromagnetism or spin glass phase. This is consistent with the results of the $M(H)$ measurements, which indicate that only the curve for the lowest temperature, i.e., T = 15 K, exhibits a hardly perceivable curvature in the low-field region near H = 0. For the magnetic moments of Ni sparsely dispersed in an alloy structure, it is not surprising to observe paramagnetism. This is currently an issue for the magnetic properties of NiPt NPs. One of the major reasons is that it is nontrivial, even currently, to synthesize high-quality crystals of NiPt alloys with homogeneous distributions of the two elements. For bulk NiPt alloys and multilayers, the FM properties have been reported [9, 23]. Experiments for NiPt NPs in FM, SPM, and PM materials have been performed with regard to the size, the shape, and more importantly, the composition ratio of Ni over Pt [13, 24]. The PM behavior for $Ni_{31}Pt_{69}$ NPs and an FM property for $Ni_{50}Pt_{50}$ NPs below 7.4 K were reported [13]. Superparamagnetism was reported for NiPt NPs [24]. As we previously demonstrated, the uniform alloying of NiPt NPs with a concentration of approximately 1:2 is PM at T > 12.5 K. However, the magnetic properties observed in experiments appear to be extrinsic, depending on synthesis processes. For $NiPt_2$ NPs of the same size, morphology, and composition synthesized via the same processes but with a different heating rate, FM behaviors were observed, which persisted to a temperature far higher than 300 K, as shown in Fig. S3 (in the ESM). We believe that the distributions of Ni within the NiPt particles might be a critical factor for the magnetic properties. In this case, Ni atoms might aggregate locally within the NiPt NP to form Ni-rich regions or even Ni nanoclusters, yielding FM behaviors. This issue will be further addressed in the other works.

Further analysis of the $M(H)$ curves for the PM sample yields some interesting results. First, the average effective moment is calculated as μ_{eff} = 0.9, 1.2, and 1.9 μ_B per atom, including Ni and Pt, at T = 15, 70, and 300 K, by applying the Langevin expression $\chi = N\mu^2_{eff}/3k_BT$. These values are on the order of only a few Bohr magnetons, supporting the observations

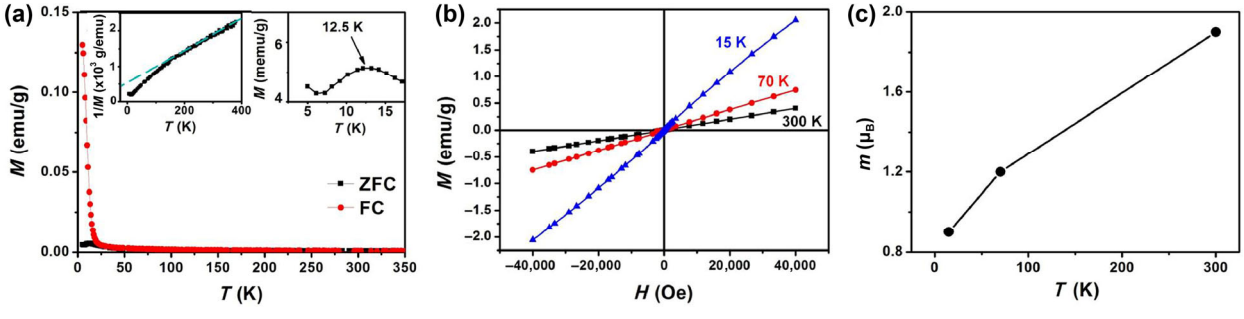

Figure 2 Magnetizations for a powder sample of $NiPt_2$ NPs with the average magnetic moments of each atom. (a) FC and ZFC $M(T)$ curves recorded in an applied magnetic field of 90 Oe. The left inset shows a plot for $1/M(T)$ vs. T, revealing the PM nature of the sample. The right inset shows the structure at 12.5 K, which is identified as the freezing temperature T_F. (b) $M(H)$ curves showing the PM behavior at 15, 70, and 300 K. (c) Magnetic moments analyzed using the $M(H)$ data for three different temperatures according to Langevin analysis, averaged over the total number of atoms, including Ni and Pt.

of PM rather than SPM properties. Second, these magnetic moments are significantly larger than the bulk Ni, 0.6 μ_B, implying that induced moments may occur with Pt atoms. This is later confirmed by DFT calculations in the present work. Third, the average magnetic moments exhibit anomalous temperature dependency compared with normal magnetic materials. A higher temperature yields a larger moment, in the range of T = 15 K to at least 300 K. Figure 2(c) shows the average magnetic moments with respect to the temperature. The results suggest a thermally activated type of behavior with electrons transferred between Ni and Pt atoms within the alloy, resulting in the increase of the magnetic moment with the temperature. This thermal activation behavior is confirmed by XANES experiments and revealed by DFT calculations, as described in later sections.

Another interesting feature revealed by the $M_{ZFC}(T)$ measurement in Fig. 2(a) is that there is a structure or a peak at T = 12.5 K (see the right inset). We consider this to be the freezing temperature (T_F) associated with the spin glass transition for the magnetic moments of Ni, rather than a blocking temperature for SMP NPs. The freezing temperature $T_F \approx 12.5$ K has also been observed with the FM $NiPt_2$ sample mentioned in the previous paragraph (see Fig. S3 in the ESM). Additionally, $T_F \approx 12$ K has been reported for pure Ni nanochains, which is identified as the freezing temperature for the surface spin glass transition of the Ni magnetic moment [25, 26].

Temperature-dependent XANES experiments were performed for the Pt L3-edge in the transmission mode, around the listed energy of 11,564 eV. Measurements were performed for both pure Pt NPs and the alloying $NiPt_2$ NPs, at increasing temperatures of T = 10, 50, 80, 150, 200, 250, and 300 K. The absorption spectra, background subtracted and normalized, for pure Pt and $NiPt_2$ NPs are shown in the separate graphs of Fig. 3(a). The Pt L3 white lines (WLs), which are the peaks at the absorption edge, for $NiPt_2$ and Pt NPs almost collapse to a single curve in the full scale of the measurements, without revealing any obvious temperature-dependent effects.

However, in a magnified scale around the peak region, a higher-order difference in the peak value becomes more obvious for these two samples at a high temperature. Figures 3(b) and 3(c) show the data points around the peaks at T = 10 and 300 K, respectively. The solid curves in the graphs are obtained by applying three-point parabolic fitting around the peak. At a low temperature, T = 10 K, there is essentially no difference between the two absorption peaks for pure Pt and $NiPt_2$ NPs (see Fig. 3(b)), whereas the peak value for the NiPt NPs is suppressed compared with that for pure Pt at T = 300 K (see Fig. 3(c)). The same analysis method is applied to obtain the results at other temperatures—50, 80, 150, 200, and 250 K—as shown in Figs. S4(a)–S4(e) (in the ESM), respectively. The difference in the peak value of the X-ray absorption intensity, ΔI, of the Pt L3 edges with pure Pt and $NiPt_2$ NPs, i.e., the data for pure Pt subtracted by those of the NiPt alloy, are plotted in Fig. 3(d). Clearly, ΔI increases with the temperature. Although the L3 near-edge spectrum probes the $2p_{3/2} \rightarrow 5d_{3/2, 5/2}$ dipole transitions, the Pt L3 near-edge spectrum, that is, WL, includes only the unoccupied $5d_{5/2}$ character, owing to the absence of the $5d_{3/2}$ holes in Pt. The increase in ΔI is attributed to the fact that electrons thermally activated from the Ni 3d orbitals occupy part of the vacancies of Pt $5d_{5/2}$, hence, suppressing the subsequent WL transition of Pt in NiPt NPs. This agrees well with the calculated results below.

DFT calculations are performed to investigate the electron distributions for the Ni 3d and Pt 5d orbitals with pure Ni, pure Pt, and Ni_1Pt_{54} clusters. The model structure for the NiPt alloying state is a truncated-octahedral Ni_1Pt_{54} cluster, as shown in Fig. 4(a). The charge-density difference at T = 0 is obtained, indicating the variations of the charge distributions for Ni 3d (or Pt 5d) orbitals in the Ni_1Pt_{54} cluster from those for pure Ni (or Pt). The results are shown in Fig. 4(b), revealing that the electron distributions decrease for Ni, which is represented by the yellow region surrounding the central Ni in Fig. 4(b), whereas they increase for the Pt atoms at the nearest neighbors, which are indicated by the blue regions in the plot. A hardly visible increase of the electron distribution for Pt at the next-nearest neighbors occurs. This indicates charge transfer from Ni to Pt atoms.

In further investigations, the projected density of states (PDOS) is obtained via DFT calculations for 1)

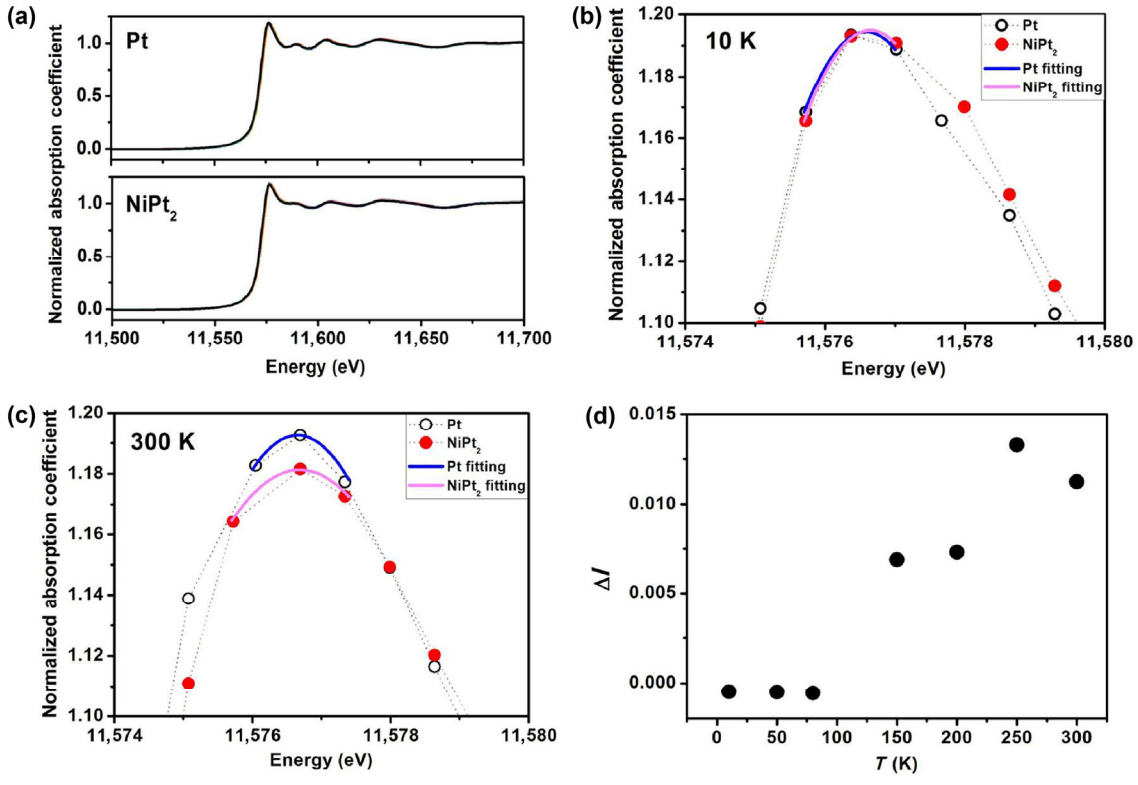

Figure 3 Temperature-dependent XANES spectra of Pt L3 edges, the $2p_{3/2} \rightarrow 5d_{5/2}$ transition, for NP samples of pure Pt and $NiPt_2$ alloys. Measurements are performed in the transmission mode at T = 10, 50, 150, 200, 250, and 300 K. (a) Normalized XANES spectra of Pt L3 edges at seven different temperatures for the pure Pt and $NiPt_2$ alloys. The absorption peaks at the Pt L3-edge in a magnified scale of (a) are plotted for pure Pt and $NiPt_2$ alloys (b) at T = 10 K and (c) at T = 300 K. The data points with connecting dotted lines represent the experimental curves. Three-point parabolic fittings around the edge peaks of absorption are indicated by the solid lines. The peak values are essentially the same at T = 10 K. In (b), at T = 300 K, the difference in the absorption intensity at the peak positions is non-negligible. (d) Difference in ΔI of Pt L3 edges for pure Pt NPs and $NiPt_2$ alloys with respect to the temperature. The results at the other five temperatures are obtained by applying the same fitting procedure that was used for (b) and (c) (see Fig. S4 in the ESM).

the Ni-3d orbitals of pure Ni and of Ni in the Ni_1Pt_{54} alloying structures, as shown in Fig. 4(c), and 2) the Pt-5d orbitals of pure Pt_{55} and the Pt nearest neighbor to Ni, as shown in Fig. 4(d). The total states available below the Fermi energy with Ni-3d in the Ni_1Pt_{54} alloy cluster decrease relative to those in pure Ni.

This indicates that the electron distributions shift in part to the neighboring Pt. In contrast, for the PDOS curve of Pt-5d in Fig. 4(d) with Ni_1Pt_{54} alloy clusters, the integral area below the Fermi energy increases. This indicates that the Pt atoms next to Ni increase in the electron distribution. The charge-transfer from Ni-3d to Pt-5d due to the hybridization between the Ni 3d and Pt 5d orbitals at T = 0 has been investigated numerically [27].

The magnetic moments of the atoms with the clusters of pure Pt_{55} and alloying Ni_1Pt_{54} are then calculated by the sum of the density of states (DOS) for electrons with spin up and spin down below the Fermi surface. For the pure Pt_{55} cluster, each moment is nearly zero (0.001–0.068 μ_B), and the overall magnitude for the whole cluster is also close to zero: approximately 0.012 μ_B. A cross-sectional view with the magnetic moment for each atom is shown in Fig. 4(e). For the Ni_1Pt_{54} cluster, the magnetic moment of the Pt atom nearest to the central Ni atom is enhanced, as shown in Fig. 4(f). Some of the magnetic moments reach 0.305 μ_B. For a single Ni atom, the total magnetic moment of the whole alloying cluster increases from approximately 2 to 3.96 μ_B.

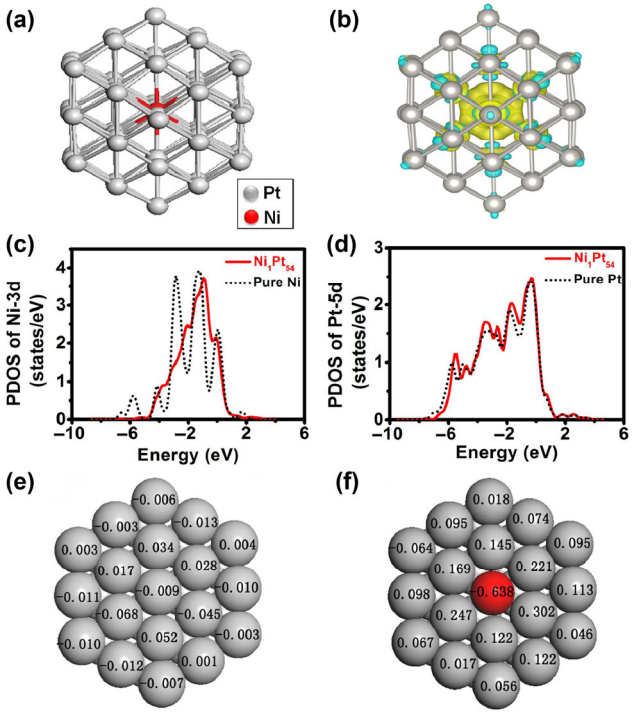

Figure 4 Calculation results showing the charge-transfer effects and the corresponding variations in the magnetic moments for a single Ni atom in the Pt cluster. (a) Structure of the Ni_1Pt_{54} cluster in the truncated-octahedral morphology. The silver spheres represent Pt, and the red one in the center represents Ni. (b) Charge-density difference for Ni_1Pt_{55} cluster in the same structure that is shown in (a). The electron distribution decreases for Ni at the center (in yellow), and the electron density increases for the Pt atoms within the next-nearest neighbors (in blue). (c) PDOS of Ni-3d for both the pure Ni_{55} (black broken curve) and the Ni_1Pt_{54} (red solid curve) alloy clusters. The lowest-energy part of DOS available for pure Ni obviously disappears after the alloying, along with the reduction in the total states available below the Fermi energy. (d) PDOS of Pt-5d for pure Pt_{55} (broken curve) and for those nearest to Ni with Ni_1Pt_{54} (solid curve) alloy clusters. (e) Magnetic moment calculated for each atom at $T = 0$ in units of Bohr magnetons, μ_B, for the pure Pt_{55} cluster and (f) the Ni_1Pt_{54} cluster. The moments of Pt nearest to Ni increase significantly, and smaller increases are obtained for the next-nearest neighbors.

Obviously, at $T = 0$, the shift of electron distributions due to the hybridization of the Ni-3d and Pt-5d orbitals leads to a significant enhancement in the magnetic moment of the alloying state. Further electron transfer due to thermal activation is therefore reasonably expected to enhance the magnetic moment, depending on the temperature. Thus, it is meaningful to calculate the energy levels of Pt-5d orbitals in pure Pt and in the NiPt alloying clusters.

To further investigate the thermal-activation effects of electrons in the alloying state, the energy levels (or molecular band structures) of the Pt-5d orbitals with and without the alloying are calculated. With the model nanocluster of 55 atoms, we determined the energy levels of the lowest unoccupied molecular orbital (LUMO) and the highest occupied molecular orbital (HOMO) specifically for the Pt-5d orbitals of a pure Pt_{55} and Ni_1Pt_{54} alloy. The results are summarized in Table 1. The schematic in Fig. 5 shows the energy levels of the HOMO and LUMO with the energy gap. Clearly, the energy gap decreases from 161 meV for the pure Pt_{55} to 38.5 meV for the Ni_1Pt_{54} alloy cluster. Thus, at $T > 0$, it is expected that the electron transfer from the HOMO to the LUMO of the Ni3d–Pt5d

Table 1 Energy gaps between the Fermi level and the HOMO (HOMO–Fermi), between the Fermi level and the LUMO (LUMO–Fermi), and between the LUMO and HOMO (LUMO–HOMO) for the molecular energy band formed by the Pt 5d-orbitals in the Pt_{55} and Ni_1Pt_{54} clusters

	LUMO–HOMO gap (eV)	HOMO–Fermi (eV)	LUMO–Fermi (eV)
Ni_1Pt_{54}	0.0385	–0.0324	0.0061
Pt_{55}	0.1610	–0.1538	0.0072

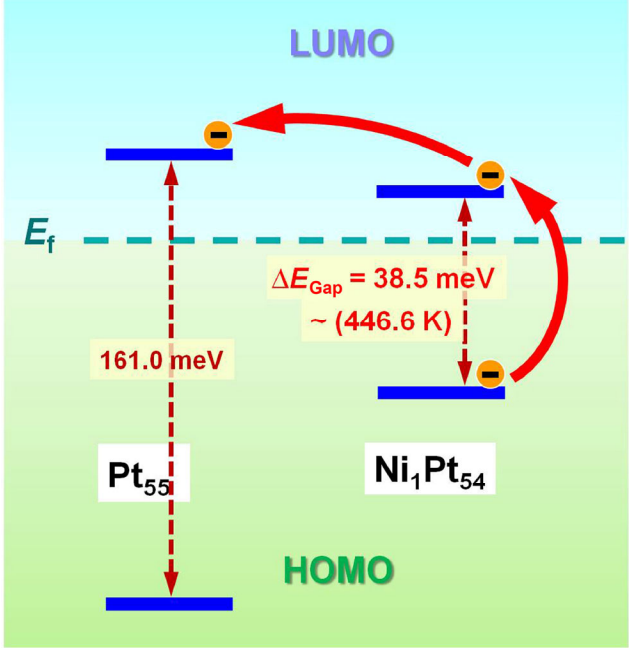

Figure 5 Schematic of thermally activated electron transfer from the energy level of the Ni_1Pt_{54} hybridized d-band orbital to that of the Pt 5d orbital.

hybridized band occurs because of thermal-activation effects, according to the Boltzmann factor, $\exp(-\Delta E/K_B T)$. This thermal-activation effect might become non-negligible at 300 K, considering that $\Delta E \approx 38.5$ meV ≈ 446.6 K. These activated electrons are then readily transferred to the nearby Pt 5d orbitals (see the diagram in Fig. 5). This explains the temperature-dependent effects of the electron transfer observed in the XANES experiment, as shown in Fig. 3(d). The magnetic moments of the atoms in the alloying states are expected to vary accordingly, which explains the anomalous temperature dependence of the magnetic moments observed in the magnetization measurements, as shown in Fig. 2(c).

There are few reports on the magnetism enhancement with the increasing temperature. Heat treatment is an effective method for increasing the saturation magnetization by approximately 15% for cobalt ferrite [28]. It is explained on the basis of cation redistribution. As another example [29], the exchange of Co cations—Co^{2+} and Co^{+}—between the A and B sites of a spinel structure can enhance the magnetism of Co_3O_4 NPs. In this case, the redistribution of the cations is attributed to the charge transfer-effect rather than the actual exchange of the cations themselves. However, in the former case, we do not know the underlying mechanism, i.e., whether the claimed "cation redistribution" is due to charge transfer or due to the actual movement of the cations.

3 Conclusions

Monodispersed single-crystal $NiPt_2$ NPs are synthesized via a simple yet general one-step solvothermal method. These NPs are truncated octahedrons in the alloying state of disordered atomic arrangements approximately 7 nm in size. PM behavior is revealed by $M(T)$ and $M(H)$ magnetization measurements. The effective magnetic moment, averaged over all atoms, including Ni and Pt, is determined as 0.9 μ_B/atom at 15 K and 1.9 μ_B/atom at 300 K. It is immensely enhanced from that of bulk nickel: 0.6 μ_B/Ni. The magnetic moment also exhibits an anomalous increase with the temperature, from 15 to 300 K. XANES experiments on the L3 edge for Pt reveal thermally activated electron transfer from the Ni 3d orbital to the Pt 5d orbital. DFT calculations indicate that the molecular bands of Pt 5d are significantly changed by the alloying with Ni. Consequently, the energy gap decreases from 161 to 38.5 meV ≈ 446.6 K of the Ni3d–Pt5d hybridized molecular band. The electrons are therefore ready to be thermally activated and transferred to the unoccupied 5d orbitals of Pt located far away from the next-nearest neighbors of the NiPt alloying centers. This provides a reasonable basis for interpreting the results of the XANES experiments on the thermally activated electron transfer and explains the anomalous temperature dependence of the magnetic moments in the $NiPt_2$ NPs.

Because of the interaction between the constituent elements, the magnetic properties of bimetallic nanomaterials are sometimes beyond the descriptions of conventional magnetics and are interesting for fundamental investigations. Moreover, the electron transfer and its thermal-activation effects in bimetallic nanomaterials are fundamental factors for their functionalities with regard to not only magnetic properties but also optic and catalytic properties. This may lead to potential applications in a wide range of areas. One potential area for applications is magnetic temperature sensors. In our opinion, this study deserves further attention in investigations of the temperature-dependent magnetic moments of bimetallic nanocrystals, in particular, a 3d metal alloying with a noble metal, such as Pt or Au.

Acknowledgements

Authors acknowledge Dr. Lirong Zheng for his XANES experimental support at the XAFS station in 1W1B beamline of BSRF and useful discussion. This work is supported by the National Natural Science Foundation of China (Nos. 11674008, 11674023, 21576008, 91334203, 51371015 and 51331002), the Beijing Natural Science Foundation (No. 2142018) and Beijing Municipal Science and Technology Project (No. Z171110000220000).

Electronic Supplementary Material: Supplementary material (chemicals and materials, synthesis methods, structural and magnetic analysis methods, XANES measurements, computational details, additional TEM

images, EDS results, additional magnetic and XANES results and supplementary references) is available in the online version of this article at https://doi.org/10.1007/s12274-017-1643-y.

References

[1] Gilroy, K. D.; Ruditskiy, A.; Peng, H. C.; Qin, D.; Xia, Y. N. Bimetallic nanocrystals: Syntheses, properties, and applications. *Chem. Rev.* **2016**, *116*, 10414–10472.

[2] Wang, D. S.; Li, Y. D. Bimetallic nanocrystals: Liquid-phase synthesis and catalytic applications. *Adv. Mater.* **2011**, *23*, 1044–1060.

[3] Huang, X. Q.; Zhao, Z. P.; Cao, L.; Chen, Y.; Zhu, E. B.; Lin, Z. Y.; Li, M. F.; Yan, A. M.; Zettl, A.; Wang, Y. M. et al. High-performance transition metal-doped Pt_3Ni octahedra for oxygen reduction reaction. *Science* **2015**, *348*, 1230–1234.

[4] Shan, A. X.; Chen, Z. C.; Li, B. Q.; Chen, C. P.; Wang, R. M. Monodispersed, ultrathin NiPt hollow nanospheres with tunable diameter and composition via a green chemical synthesis. *J. Mater. Chem. A* **2015**, *3*, 1031–1036.

[5] Dubau, L.; Nelayah, J.; Moldovan, S.; Ersen, O.; Bordet, P.; Drnec, J.; Asset, T.; Chattot, R.; Maillard, F. Defects do catalysis: CO monolayer oxidation and oxygen reduction reaction on hollow PtNi/C nanoparticles. *ACS Catal.* **2016**, *6*, 4673–4684.

[6] Alloyeau, D.; Ricolleau, C.; Mottet, C.; Oikawa, T.; Langlois, C.; Le Bouar, Y.; Braidy, N.; Loiseau, A. Size and shape effects on the order–disorder phase transition in CoPt nanoparticles. *Nat. Mater.* **2009**, *8*, 940–946.

[7] Chiang, I. C.; Chen, D. H. Synthesis of monodisperse FeAu nanoparticles with tunable magnetic and optical properties. *Adv. Funct. Mater.* **2007**, *17*, 1311–1316.

[8] Beille, J.; Bloch, D.; Besnus, M. J. Itinerant ferromagnetism and susceptibility of nickel-platinum alloys. *J. Phys. F: Metal. Phys.* **1974**, *4*, 1275–1284.

[9] Parra, R. E.; Cable, J. W. Neutron study of magnetic-moment distribution in Ni-Pt alloys. *Phys. Rev. B* **1980**, *21*, 5494–5504.

[10] Alberts, H. L.; Beille, J.; Bloch, D.; Wohlfarth, E. P. Ferromagnetic properties at high fields and high-pressures of nickel-platinum alloys near the critical concentration for ferromagnetism. *Phys. Rev. B* **1974**, *9*, 2233–2243.

[11] Kumar, U.; Mukhopadhyay, P. K.; Sanyal, B.; Eriksson, O.; Nordblad, P.; Paudyal, D.; Tarafder, K.; Mookerjee, A. Experimental and theoretical study of annealed Ni-Pt alloys. *Phys. Rev. B* **2006**, *74*, 064401.

[12] Kumar, U.; Padmalekha, K. G.; Mukhopadhyay, P. K.; Paudyal, D.; Mookerjee, A. Magnetic transition in NiPt alloy systems: Experiment and theory. *J. Magn. Magn. Mater.* **2005**, *292*, 234–240.

[13] Ahrenstorf, K.; Albrecht, O.; Heller, H.; Kornowski, A.; Görlitz, D.; Weller, H. Colloidal synthesis of Ni_xPt_{1-x} nanoparticles with tuneable composition and size. *Small* **2007**, *3*, 271–274.

[14] Zitoun, D.; Respaud, M.; Fromen, M. C.; Casanove, M. J.; Lecante, P.; Amiens, C.; Chaudret, B. Magnetic enhancement in nanoscale CoRh particles. *Phys. Rev. Lett.* **2002**, *89*, 037203.

[15] Zhang, D. F.; Zhang, Q.; Huang, W. F.; Guo, L.; Chen, W. M.; Chu, W. S.; Chen, C. P.; Wu, Z. Y. Low-temperature fabrication of Au-Co cluster mixed nanohybrids with high magnetic moment of Co. *ACS Appl. Mater. Interfaces* **2012**, *4*, 5643–5649.

[16] Dupuis, V.; Khadra, G.; Linas, S.; Hillion, A.; Gragnaniello, L.; Tamion, A.; Tuaillon-Combes, J.; Bardotti, L.; Tournus, F.; Otero, E. et al. Magnetic moments in chemically ordered mass-selected CoPt and FePt clusters. *J. Magn. Magn. Mater.* **2015**, *383*, 73–77.

[17] Bhagat, S. M.; Lucas, C. W., Jr. New technique for measurement of the temperature dependence of the saturation magnetization-nickel. *Rev. Sci. Instrum.* **1968**, *39*, 255–256.

[18] Wu, H.; Zhang, R.; Liu, X. X.; Lin, D. D.; Pan, W. Electrospinning of Fe, Co, and Ni nanofibers: Synthesis, assembly, and magnetic properties. *Chem. Mater.* **2007**, *19*, 3506–3511.

[19] Neugebauer, C. A. Temperature dependence of the saturation magnetization of nickel films of thickness less than 100a. *J. Appl. Phys.* **1960**, *31*, S152–S153.

[20] Huang, L. F.; Shan, A. X.; Li, Z. P.; Chen, C. P.; Wang, R. M. Phase formation, magnetic and optical properties of epitaxially grown icosahedral Au@Ni nanoparticles with ultrathin shells. *CrystEngComm* **2013**, *15*, 2527–2531.

[21] Billas, I. M. L.; Châtelain, A.; De Heer, W. A. Magnetism from the atom to the bulk in iron, cobalt, and nickel clusters. *Science* **1994**, *265*, 1682–1684.

[22] Wang, D. L.; Xin, H. L.; Hovden, R.; Wang, H. S.; Yu, Y. C.; Muller, D. A.; DiSalvo, F. J.; Abruña, H. D. Structurally ordered intermetallic platinum-cobalt core–shell nanoparticles with enhanced activity and stability as oxygen reduction electrocatalysts. *Nat. Mater.* **2013**, *12*, 81–87.

[23] Wilhelm, F.; Poulopoulos, P.; Srivastava, P.; Wende, H.; Farle, M.; Baberschke, K.; Angelakeris, M.; Flevaris, N. K.; Grange, W.; Kappler, J. P. et al. Magnetic anisotropy energy and the anisotropy of the orbital moment of Ni in Ni/Pt multilayers. *Phys. Rev. B* **2000**, *61*, 8647–8650.

[24] Mandal, M.; Kundu, S.; Sau, T. K.; Yusuf, S. M.; Pal, T. Synthesis and characterization of superparamagnetic Ni-Pt nanoalloy. *Chem. Mater.* **2003**, *15*, 3710–3715.

[25] He, L.; Zheng, W. Z.; Zhou, W.; Du, H. L.; Chen, C. P.; Guo, L. Size-dependent magnetic properties of nickel nanochains. *J. Phys.: Condens. Matter* **2007**, *19*, 036216.

[26] Zhou, W.; He, L.; Cheng, R.; Guo, L.; Chen, C. P.; Wang, J. L. Synthesis of Ni nanochains with various sizes: The magnetic and catalytic properties. *J. Phys. Chem. C* **2009**, *113*, 17355–17358.

[27] Zhao, F. F.; Liu, C.; Wang, P.; Huang, S. P.; Tian, H. P. First-principles investigations of the structural, electronic, and magnetic properties of $Pt_{13-n}Ni_n$ clusters. *J. Alloys Compd.* **2013**, *577*, 669–676.

[28] Nlebedim, I. C.; Melikhov, Y.; Jiles, D. C. Temperature dependence of magnetic properties of heat treated cobalt ferrite. *J. Appl. Phys.* **2014**, *115*, 043903.

[29] Chen, W. M.; Chen, C. P.; Guo, L. Field-dependent low-field enhancement in effective paramagnetic moment with nanoscaled Co_3O_4. *J. Appl. Phys.* **2010**, *108*, 073907.